

A modular-bias-sin chaotification method for enhanced discrete memristor chaotic maps

Shu Yi(易澍), Huihai Wang(王会海), and Kehui Sun(孙克辉)
Citation: Chin. Phys. B, 2026, 35 (**7**): 070504. DOI: 10.1088/1674-1056/ae181e
http://cpb.iphy.ac.cn; http://iopscience.iop.org/cpb

What follows is a list of articles you may be interested in

Fixed points as regulatory hubs in discrete memristive neural networks: An analysis of the FitzHugh-Nagumo model

Shaobo He(贺少波), Jiawei Xiao(肖佳伟), Qilai Chen(陈祺来), and Huihai Wang(王会海)
Chin. Phys. B, 2026, 35 (**6**): 060502. DOI: 10.1088/1674-1056/ae3131

Dynamics analysis and DSP implementation of the Rulkov neuron model with memristive synaptic crosstalk

Yichen Bi(毕毅晨), Jun Mou(牟俊), Herbert Ho-Ching Iu, Nanrun Zhou(周南润), Santo Banerjee, and Suo Gao(高锁)
Chin. Phys. B, 2026, 35 (**1**): 010504. DOI: 10.1088/1674-1056/ae1728

Dynamical behavior of ring-star neural networks with small-world characteristics

Minglin Ma(马铭磷), Zhiyi Yuan(袁芷依), Umme Kalsoom, Weizheng Deng(邓为政), and Shaobo He(贺少波)
Chin. Phys. B, 2025, 34 (**10**): 100502. DOI: 10.1088/1674-1056/adde39

A novel non-autonomous hyperchaotic map based on discrete memristor parallel connection

Weiping Wu(吴伟平), Mengjiao Wang(王梦蛟), and Qigui Yang(杨启贵)
Chin. Phys. B, 2025, 34 (**5**): 050503. DOI: 10.1088/1674-1056/adb8bc

The dynamics of a memristor-based Rulkov neuron with fractional-order difference

Yan-Mei Lu(卢艳梅), Chun-Hua Wang(王春华), Quan-Li Deng(邓全利), and Cong Xu(徐聪)
Chin. Phys. B, 2022, 31 (**6**): 060502. DOI: 10.1088/1674-1056/ac539a

---

A modular-bias-sin chaotification method for enhanced discrete memristor chaotic maps

Shu Yi(易澍)[1], Huihai Wang(王会海)[2,†], and Kehui Sun(孙克辉)[3]

[1] *School of Microelectronics, Tianjin University, Tianjin* 300354, *China*
[2] *School of Electronics Information, Central South University, Changsha* 410083, *China*
[3] *School of Physics, Central South University, Changsha* 410083, *China*

(Received 10 September 2025; revised manuscript received 21 October 2025; accepted manuscript online 28 October 2025)

This paper proposes a novel modular-bias-sin chaotification method (MBSC) to address the limitations of existing discrete memristor (DM)-based chaotic maps. By applying MBSC to several fundamental discrete memristors, the enhanced chaotic variants are constructed. Comprehensive dynamical analyses, including attractor phase diagrams, Lyapunov exponents, bifurcation diagrams, Shannon entropy (SE) complexity, and chaotic region scale (CRS), demonstrate that the MBSC-enhanced maps outperform the original DM maps and existing modified models. Specifically, they exhibit wider chaotic parameter ranges, larger Lyapunov exponents, higher SE complexity, and robust hyperchaotic behavior. To validate practical applicability, a pseudo-random number generator (PRNG) based on the enhanced chaotic maps is implemented, which passes all NIST SP 800-22 statistical tests, confirming its high randomness and suitability for security-sensitive applications.

Keywords: discrete memristor, chaotification method, dynamical analyses, pseudo-random number generator

PACS: 05.45.–a, 84.30.–r, 05.45.Pq

DOI: 10.1088/1674-1056/ae181e **CSTR:** 32038.14.CPB.ae181e

1. Introduction

Professor Leon Chua predicted the memristor as the fourth fundamental electronic component following resistors, capacitors, and inductors in 1971,[1] with its first realization achieved in 2008.[2] The memristor enables precise control over its characteristics via charge and magnetic flux. Endowed with inherent nonlinear memristive properties, non-volatile storage capabilities, and synaptic plasticity, it has been applied in various fields such as non-volatile memory,[3,4] artificial intelligence,[5,6] nervous system,[7–9] chaotic dynamics,[10–12] and secure communication.[13] Compared with continuous memristors, discrete memristors feature a simplified system architecture, a more straightforward structure, ease of implementation, enhanced digital compatibility, and lower implementation costs on digital platforms. In 2020, Peng *et al.* developed a DM model and applied it to the Hénon map.[14] Since then, a growing number of DM-based chaotic maps have been proposed, including fractional memristive discrete maps,[15] quadratic discrete memristors (Q-DM), sinusoidal discrete memristors (S-DM), exponential discrete memristors (E-DM), and absolute value discrete memristors (A-DM).[16] As a result, they have shown potential in digital systems,[17] image encryption,[18–20] secure communication,[21] neuron network,[22,23] and resource-constrained application scenarios,[24] prompting extensive research by scholars in the field.

Discrete memristors exhibit unique nonlinear characteristics due to their internal state variables, which distinguish them from traditional nonlinear devices and also facilitate the construction of chaotic maps. To enhance the dynamical performance of systems, researchers often combine DMs with existing chaotic maps or systems to improve their dynamical properties. In 2021, Bao *et al.* applied Q-DM to the logistic map and introduced cosine discrete memristors into different maps, both of which effectively enhanced the chaotic performance and created new maps with higher complexity.[25,26] Ma *et al.* proposed a locally active DM and applied it to a two-dimensional chaotic map.[27] In 2022, Liang *et al.* developed a discrete memristive chaotic map exhibiting line fixed points, multistability, and enhanced chaotification.[28] In 2023, Fu *et al.* developed a divergence-free memristive Hénon map using state variable difference, demonstrating rich dynamics and physical realizability through circuit implementation.[29] In 2024, Wang *et al.* proposed a fractional-order memristive Hénon map with wider chaotic range and order-dependent dynamics, and successfully implemented it on an FPGA platform.[30] In 2025, Wu *et al.* proposed a non-autonomous DM-based hyperchaotic map with "initial-boosted attractors" and "attractor size control", confirming its potential in enhancing chaotic complexity.[31]

In recent studies, researchers have leveraged the intrinsic nonlinearity of memristors to develop novel chaotic maps through self-feedback approaches. Bao *et al.* established a

†Corresponding author. E-mail: wanghuihai_csu@csu.edu.cn

© 2026 Chinese Physical Society and IOP Publishing Ltd. All rights, including for text and data mining, AI training, and similar technologies, are reserved.

generalized DM model and derived four hyperchaotic maps exhibiting initial-sensitive characteristics in 2021.[16] Building upon it, subsequent advancements, including their development of quadratic DM cascade and parallel architectures, comprehensively characterized parameter-dependent dynamical behaviors.[32,33] Further progress was achieved by Yuan *et al*. through innovative DM operational methodologies involving cascade, parallel, and composite configurations in 2023.[34] In 2022, Deng *et al*. implemented a simplified DM map for reservoir computing applications.[35] Yu *et al*. proposed a novel cosine hyperchaotic map with multiple amplitude control modes and boosting-free regions in 2024.[36] Notably, Zhu *et al*. introduced a modular arithmetic approach for DM chaotic enhancement, significantly improving dynamical performance.[37] Despite these advancements, critical challenges persist regarding constrained chaotic domains, limited Lyapunov exponents and inadequate complexity factors contributing to predictable parameter sensitivity and instability under perturbations.[38–40] This limitation underscores the fundamental trade-off between performance and complexity in the design of chaotic systems. As a result, current research efforts concentrate on developing robust chaotic maps that balance these conflicting requirements while preserving enhanced dynamical characteristics.

This paper presents a novel modular-bias-sin chaotification method (MBSC) that significantly enhances the chaotic characteristics of conventional memristor maps through the synergistic integration of self-feedback mechanisms, modular arithmetic operations, and trigonometric (sine) transformations. The proposed MBSC approach is systematically applied to four fundamental memristor maps, successfully generating four distinct chaotic variants with markedly improved nonlinear dynamics. Comprehensive dynamical analyses and comparative studies with existing methods demonstrate that the novel maps exhibit superior chaotic performance across multiple metrics, including wider parameter ranges for chaotic behavior, significantly larger Lyapunov exponents, enhanced SE complexity, and expanded chaotic parameter scales. These quantitative improvements collectively validate the effectiveness of the MBSC method in substantially augmenting the chaotic properties of memristor-based maps while maintaining implementation feasibility, offering promising potential for applications requiring robust chaotic behavior.

The remainder of this paper is organized as follows. Section 2 provides a comprehensive review of discrete memristors and introduces the proposed MBSC methodology in detail. In Section 3, we conduct a thorough analysis of the chaotic dynamical characteristics of the enhanced maps and perform comparative studies with existing approaches. Section 4 presents a pseudo-random number generator (PRNG) based on the enhanced chaotic maps, and validates the randomness quality using the NIST statistical test. Its practicality is verified through space complexity, time complexity, and throughput tests. Finally, Section 5 concludes the paper by summarizing key findings and discussing potential applications.

2. Chaotification method for discrete memristors

2.1. Discrete memristors

A memristor, as the fourth fundamental circuit element following resistors, capacitors, and inductors, exhibits intrinsic nonlinear characteristics. The mathematical model of a continuous memristor is expressed as follows:

$$\begin{cases} v(t) = M(q)i(t), \\ \frac{\mathrm{d}q(t)}{\mathrm{d}t} = i(t), \end{cases} \tag{1}$$

where $v(t)$ and $i(t)$ denote voltage and current respectively, q represents the charge, and $M(q)$ stands for the memristance, a state-dependent function determined by the charge q. Through the application of the forward Euler difference method, the continuous memristor can be discretized to derive the discrete memristor, whose mathematical expression is given by

$$\begin{cases} v_n = M(q_n)\, i_n, \\ q_{n+1} = q_n + \varepsilon i_n, \end{cases} \tag{2}$$

where v_n, i_n, q_n and $M(q_n)$ represent the voltage, current, charge and memristance at the n-th iteration, respectively. $M(q_n)$ has many types and is expressed in different mathematical expressions. ε is a scaling factor, but for simplicity, its value will be set to 1 in the subsequent analysis. Four commonly used discrete memristor models are listed in Table 1, including Q-DM, A-DM, S-DM, and E-DM. Usually, these memristors can form a memristor chaotic map through self-feedback operation.[16] It is noteworthy that the maps tend to diverge easily under signal stimulation and exhibit only limited chaotic behavior. In this study, a novel chaotification method is proposed to enhance their chaotic performance.

2.2. Design of the modular chaotification method

To address these issues, we propose a novel chaotification approach, namely, the modular-bias-sin chaotification method (MBSC). In order to distinguish it from variables that originally had a practical physical concept, we replace v with x. The mathematical expression of the MBSC chaotic map is as follows:

$$\begin{cases} x_{n+1} = [aM(q_n)x_n + b] \mod m, \\ q_{n+1} = k\sin(x_n + q_n), \end{cases} \tag{3}$$

where a denotes the scaling factor from the original discrete memristive map. Its function is to adjust the amplitude of the output of the memristor. b is the bias parameter. m represents the modulus, and k is the scaling factor for the introduced sin

function. x_n and q_n correspond to the sequence values at the n-th iteration. The method constructs new chaotic maps through three key modifications: modular arithmetic constrains the variable range to prevent numerical overflow, a bias parameter fine-tunes the system state to eliminate stable points, and the sin function introduces additional nonlinearity to enhance chaotic complexity. The structure of the MBSC is illustrated more clearly in Fig. 1. By inputting only the initial values x_0 (iterative sequence initial value) and q_0 (memristor initial state), the system automatically performs iterative computation and outputs two sequences x_{n+1} and q_{n+1}. In addition, D in Fig. 1 represents a delay unit of the iterative map. That is, after a delay time, x_{n+1} replaces x_n for the next iteration calculation. In order to demonstrate the generality of the proposed method and facilitate comparative analysis, this paper continues to use the four discrete memristors from Refs. [16,37], as shown in Table 1.

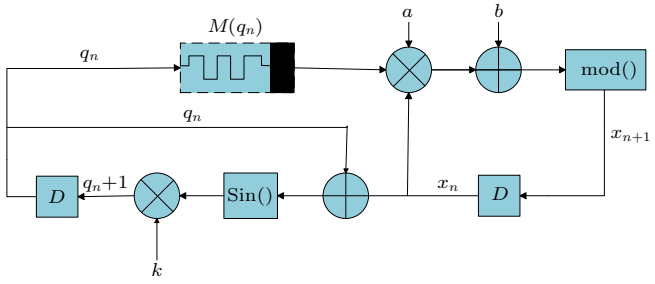


Fig. 1. The structure of the MBSC method.

Table 1. Mathematical expression of the four DMs and corresponding MBSC.

DM	Mathematical expression	MBSC	Mathematical expression
Q-DM	$\begin{cases} x_{n+1} = a\left(q_n^2 - 1\right) x_n \\ q_{n+1} = q_n + x_n \end{cases}$	Q-MBSC	$\begin{cases} x_{n+1} = [a(q_n^2 - 1)x_n + b] \bmod m \\ q_{n+1} = k\sin(x_n + q_n) \end{cases}$
A-DM	$\begin{cases} x_{n+1} = a\left(\lvert q_n\rvert - 1\right) x_n \\ q_{n+1} = q_n + x_n \end{cases}$	A-MBSC	$\begin{cases} x_{n+1} = [a\left(\lvert q_n\rvert - 1\right) x_n + b] \bmod m \\ q_{n+1} = k\sin(x_n + q_n) \end{cases}$
S-DM	$\begin{cases} x_{n+1} = a\sin\left(\pi q_n\right) x_n \\ q_{n+1} = q_n + x_n \end{cases}$	S-MBSC	$\begin{cases} x_{n+1} = [a\sin\left(\pi \cdot q_n\right) x_n + b] \bmod m \\ q_{n+1} = k\sin(x_n + q_n) \end{cases}$
E-DM	$\begin{cases} x_{n+1} = a(\mathrm{e}^{-\cos(\pi q_n)} - 1)x_n \\ q_{n+1} = q_n + x_n \end{cases}$	E-MBSC	$\begin{cases} x_{n+1} = [a(\mathrm{e}^{-\cos(\pi q_n)} - 1)x_n + b] \bmod m \\ q_{n+1} = k\sin(x_n + q_n) \end{cases}$

3. Dynamical characteristics analysis

3.1. Attractor phase diagram

An attractor refers to the long-term stable trajectory of a chaotic system in the phase space, reflecting the intrinsic laws of the system. Phase diagram analysis provides an intuitive means to preliminarily determine whether a system is in a chaotic state. Figure 2 illustrates the phase diagram of the Q-MBSC attractor under the following Parameter configurations: $a = 3$, $b = 1$, initial values $x_0 = 0.1$ and $q_0 = 0.1$, along with two distinct parameter pairs: $k = 2$, $m = 5$ and $k = 5$, $m = 2$. These phase diagram illustrate that m controls the range of $x_n \in (0, m)$ in the phase space, while k governs the range of $q_n \in (-k, k)$. In Fig. 2(a), when $k = 5$ and $m = 2$, the range of q_n is $(-5, 5)$, and the range of x_n is (0, 2). In Fig. 2(b), when $k = 2$ and $m = 5$, the range of q_n is $(-2, 2)$, and the range of x_n is (0, 5). Additionally, the state points of the chaotic system

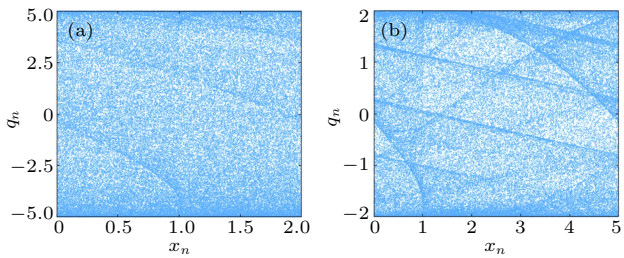


Fig. 2. The phase diagram of the Q-MBSC attractor: (a) $k = 5$, $m = 2$, (b) $k = 2$, $m = 5$.

are observed to be uniformly distributed across the attractor domain in two phase diagrams, indicating that the system exhibits excellent ergodicity. Considering the control effects of k and m in Eq. (3), the attractors of the x_n–q_n plane for the four MBSC maps in Table 1 should be similar to Fig. 2. This has also been confirmed through simulation, so the attractors for the other three MBSC maps are not shown in the paper.

3.2. Lyapunov exponents and bifurcation diagrams

In this section, we sequentially analyze the Lyapunov exponents and bifurcation diagrams of the chaotic maps under different parameter conditions, with comparisons to previous research findings. We begin with parameter a. Figure 3 presents the Lyapunov exponents and bifurcation diagrams of MBSC maps under the parameter settings: $b = 1$, $k = 5$, $m = 2$, initial values $x_0 = 0.1$ and $q_0 = 0.1$, and $a \in [0, 6]$. For comparison, Fig. 4 shows the analysis results of previous studies under the same parameter conditions. Q-MBC, A-MBC, S-MBC, and E-MBC represent the chaotic maps obtained by applying the chaotification method from Ref. [37] to the four fundamental memristors, respectively. For comparison purposes, we replot the figures from the aforementioned reference here. As observed from Fig. 3, the Lyapunov exponents increase gradually with the growth of parameter a, and their values are consistently larger than those shown in Fig. 4. For comparative analysis, we examine the Q-MBSC and Q-MBC cases. As

shown in the figure, when $a = 6$, the Lyapunov exponent of MBSC approaches 4, whereas that of MBC remains around only 2. In contrast, Fig. 4 reveals that as a increases, distinct periodic windows emerge, and the bifurcation diagram shows transitions from chaotic to periodic states, whereas the MBSC maps exhibit only periodic behavior near $a = 0$ as shown in Fig. 3. For most of the parameter range, the MBSC maps maintain chaotic or hyperchaotic states.

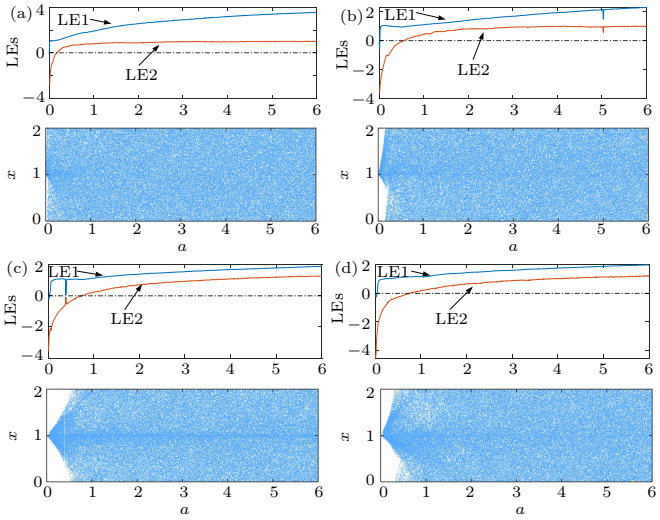


Fig. 3. The Lyapunov exponents and bifurcation diagrams of MBSC maps with $b = 1$, $k = 5$, $m = 2$, $x_0 = 0.1$ and $q_0 = 0.1$: (a) Q-MBSC map, (b) A-MBSC map, (c) S-MBSC map, (d) E-MBSC map.

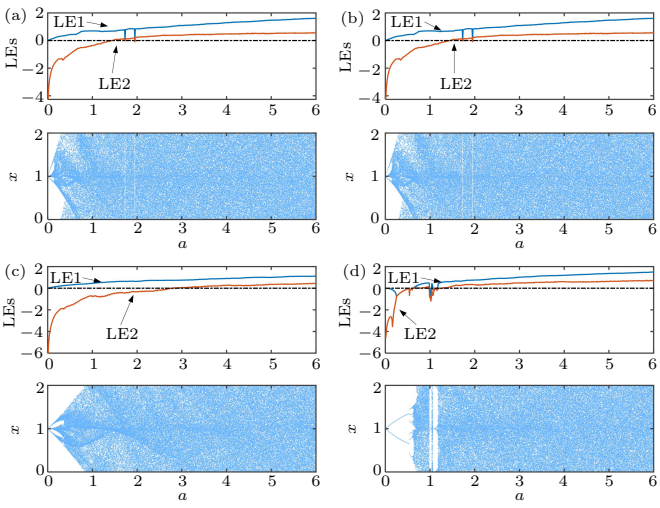


Fig. 4. The Lyapunov exponents and bifurcation diagrams of MBC maps with $b = 1$, $m = 2$, $x_0 = 0.1$ and $q_0 = 0.1$: (a) Q-MBC map, (b) A-MBC map, (c) S-MBC map, (d) E-MBC map.

Next, we turn to parameter b, which functions as the bias parameter in Eq. (3). Its primary role is to eliminate stable points in the original system and enhance the system's chaotic characteristics. Figure 5 presents the Lyapunov exponents and bifurcation diagrams of MBSC maps under the parameter configuration: $a = 3$, $k = 5$, $m = 2$, initial values $x_0 = 0.1$ and $q_0 = 0.1$, with $b \in [-5,5]$. As observed from the figures, throughout the variation of b, the system exhibits significant chaotic behavior: both Lyapunov exponents remain consistently positive with minimal fluctuations, indicating that the map maintains a hyperchaotic state. Figure 6 displays the Lyapunov exponents and bifurcation diagram of the MBC maps under identical parameter conditions. It can be observed that periodic windows emerge in the MBC maps, leading to a transition from chaotic to non-chaotic states. In comparison with the results in Fig. 6, the MBSC demonstrates higher Lyapunov exponents across the entire range of b, with periodic windows completely absent. This confirms stronger stability in its chaotic behavior, further validating the superiority of MBSC in enhancing chaotic characteristics.

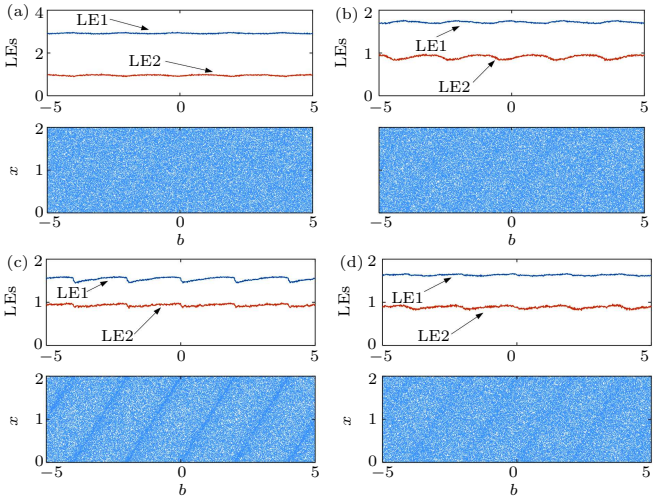


Fig. 5. The Lyapunov exponents and bifurcation diagrams of MBSC maps with $a = 3$, $k = 5$, $m = 2$, $x_0 = 0.1$ and $q_0 = 0.1$: (a) Q-MBSC map, (b) A-MBSC map, (c) S-MBSC map, (d) E-MBSC map.

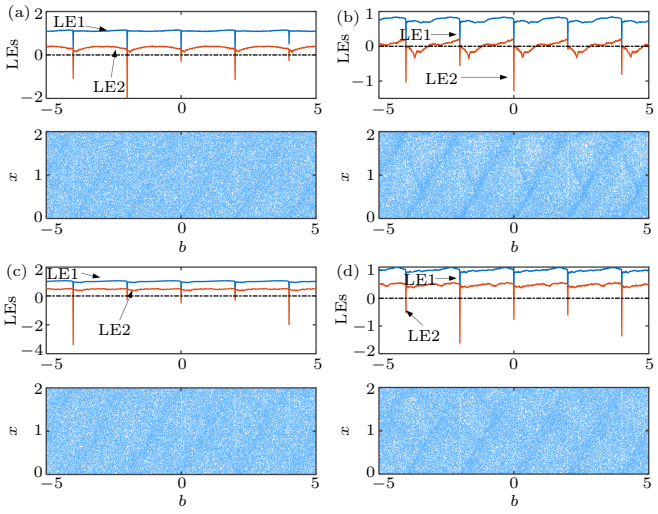


Fig. 6. The Lyapunov exponents and bifurcation diagrams of MBC maps with $a = 3$, $m = 2$, $x_0 = 0.1$ and $q_0 = 0.1$: (a) Q-MBC map, (b) A-MBC map, (c) S-MBC map, (d) E-MBC map.

Subsequently, we examine parameter m, which corresponds to the modulus in the proposed method. This parameter restricts the range of the attractor domain and influences the system's dynamical behavior. Figure 7 presents the Lyapunov exponents and bifurcation diagrams of MBSC maps under the parameter settings: $a = 3$, $b = 1$, $k = 5$, initial values $x_0 = 0.1$ and $q_0 = 0.1$, with $m \in [0,10]$. It can be observed that the maximum Lyapunov exponent (MLE) of the Q-MBSC, A-MBSC,

and E-MBSC remains consistently positive, while the second Lyapunov exponent (LE2) exhibits a gradual upward trend, indicating that these systems maintain chaotic or hyperchaotic states throughout the parameter range. For the S-MBSC, transient periodic windows appear only near $m = 0$ and $m = 1$, with chaotic behavior preserved in all other ranges. Figure 8 shows the Lyapunov exponents and the bifurcation diagrams of the MBC maps under identical parameter conditions. However, the chaotic characteristics under this configuration are unsatisfactory, particularly when m is small, where the system exhibits a relatively low Lyapunov exponent accompanied by pronounced unstable oscillations. In comparison with Fig. 8, the Lyapunov exponents of the MBSC are significantly enhanced. This is particularly evident in the A-MBC: in Fig. 8, the Lyapunov exponent decreases gradually with increasing m and even becomes negative, whereas the A-MBSC map maintains a high Lyapunov exponent and retains a hyperchaotic state across the entire range, demonstrating stronger stability in its chaotic behavior. It should be additionally noted that in the four bifurcation diagrams in Fig. 7, when $m \in [0, 10]$, the amplitude of the maximum value of the sequence x_n linearly increases from 0 to 10. The maximum value of x_n is equal to m. This is exactly consistent with the conclusion in Subsection 3.1 that m controls the range of $x_n \epsilon (0, m)$ in the phase space.

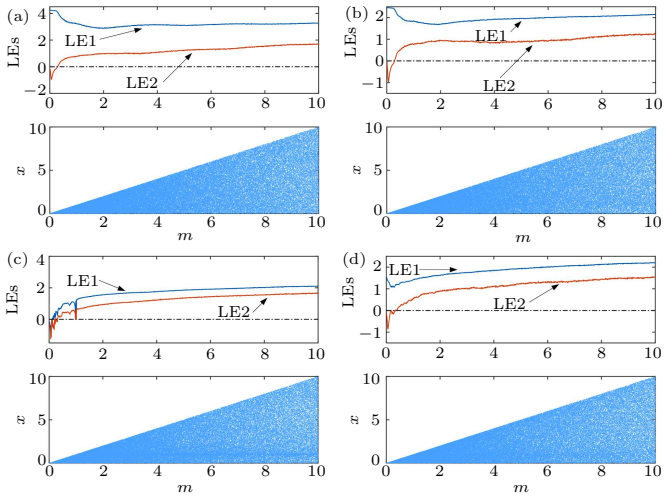


Fig. 7. The Lyapunov exponents and bifurcation diagrams of MBSC maps with $a = 3$, $k = 5$, $b = 1$, $x_0 = 0.1$ and $q_0 = 0.1$: (a) Q-MBSC map, (b) A-MBSC map, (c) S-MBSC map, (d) E-MBSC map.

Comparing Figs. 3 and 4, Figs. 5 and 6, as well as Figs. 7 and 8 obtained from numerical simulations, there are some points where chaotic performance has decreased. But overall, the majority of Lyapunov exponents have improved, with many areas being in a hyperchaotic state and the chaotic range significantly increasing, especially eliminating all the periodic windows in Fig. 6. So, the introduction of the variables has improved the overall chaotic performance of the map.

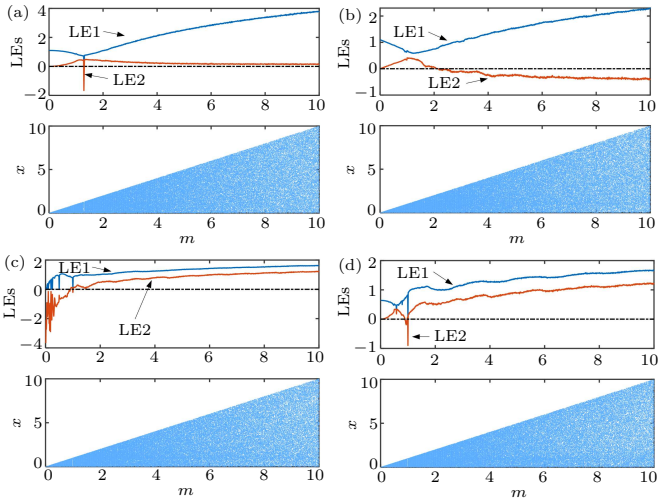


Fig. 8. The Lyapunov exponents and bifurcation diagrams of MBC maps with $a = 3$, $b = 1$, $x_0 = 0.1$ and $q_0 = 0.1$: (a) Q-MBC map, (b) A-MBC map, (c) S-MBC map, (d) E-MBC map.

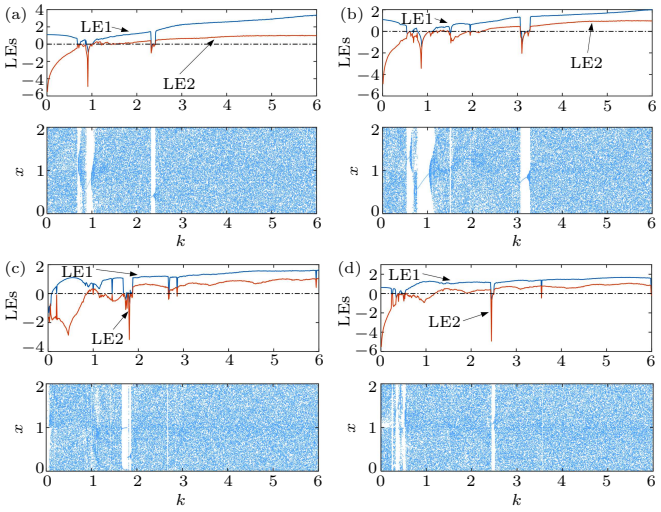


Fig. 9. The Lyapunov exponents and bifurcation diagrams of MBSC maps with $a = 3$, $b = 1$, $m = 2$, $x_0 = 0.1$ and $q_0 = 0.1$: (a) Q-MBSC map, (b) A-MBSC map, (c) S-MBSC map, (d) E-MBSC map.

Moving on to parameter k, which acts as a control parameter in the MBSC method to regulate the system's dynamic equilibrium, we further analyze its influence. Figure 9 presents the Lyapunov exponents and bifurcation diagrams of MBSC maps under the parameter configuration: $a = 3$, $b = 1$, $m = 2$, initial values $x_0 = 0.1$ and $q_0 = 0.1$, with $k \in [1, 10]$. The results indicate that as k increases, the system's Lyapunov exponents exhibit a gradual upward trend, reflecting a continuous enhancement of chaotic characteristics. However, transient periodic windows are observed, for instance, in the A-MBSC, these windows are primarily concentrated near $k = 1$ and $k = 3$, with chaotic behavior maintained throughout the remaining range. In Fig. 9, which shows the Lyapunov exponents and bifurcation diagrams of MBSC maps, multiple periodic windows appear as k changes. Performance degradations occur. This is mainly due to the characteristics of different discrete memristors. In order to maintain good chaotic

characteristics of the system in applications, it is necessary to comprehensively consider the selection of parameters.

Finally, we investigate the effects of variations in initial values x_0 and q_0 to determine whether the system can maintain a stable chaotic state under such changes. Figure 10 presents the Lyapunov exponents of MBSC maps under the parameter settings: $a = 3$, $b = 1$, $m = 2$, $k = 5$, with $x_0 \in [-3,3]$ and $q_0 \in [-2,2]$. As observed, the Lyapunov exponents of the MBSC remain consistently high with minimal fluctuations across all variations of x_0 and q_0, indicating strong robustness against initial value perturbations. Additionally, both Lyapunov exponents remain positive throughout the entire range, confirming that the system maintains a stable hyperchaotic state under different initial conditions. In contrast, the Lyapunov exponents shown in Ref. [37] are smaller, and for the A-MBC in particular, the second Lyapunov exponent becomes negative, failing to sustain a hyperchaotic state. These results further validate the superiority of the proposed method under initial value perturbations, ensuring the system's stability and reliability across diverse initial conditions.

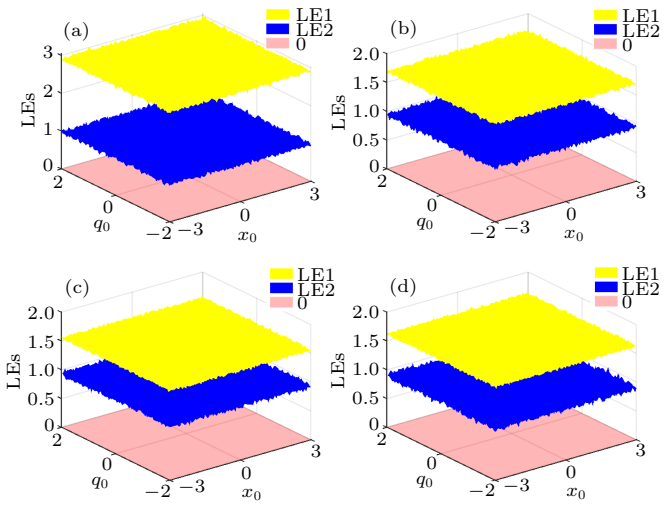


Fig. 10. The Lyapunov exponents of MBSC maps with $a = 3$, $b = 1$, $m = 2$, $k = 5$: (a) Q-MBSC map, (b) A-MBSC map, (c) S-MBSC map, (d) E-MBSC map.

3.3. SE complexity

SE complexity is an indicator used to measure the randomness of output sequences of the system: the closer its value is to 1, the more random the sequence, and the more difficult it is to be cracked or predicted. Below is a detailed analysis of SE complexity for MBSC maps under different parameter conditions.

When the parameters are set as $a = 3$, $b = 1$, $k = 5$, $m = 2$, with $x_0 \in [-3,3]$ and $q_0 \in [-2,2]$, the SE complexity of different maps is shown in Fig. 11. As observed, the SE complexity of the proposed model remains consistently above 0.94 across all variations of initial values x_0 and q_0, indicating extremely high randomness and anti-prediction capability.

Figure 12 presents the heatmap of the system's SE complexity under the parameter settings: $k = 5$, $m = 2$, $x_0 = 0.1$, $q_0 = 0.1$, with $a \in [0,10]$ and $b \in [0,10]$. From Fig. 12, it can be seen that the system exhibits low SE complexity only under a few parameter combinations, and in most regions, the SE complexity remains above 0.9. This demonstrates that the system maintains high randomness and strong anti-prediction capability over a wide range of parameters, further confirming the superiority and applicability of the proposed model.

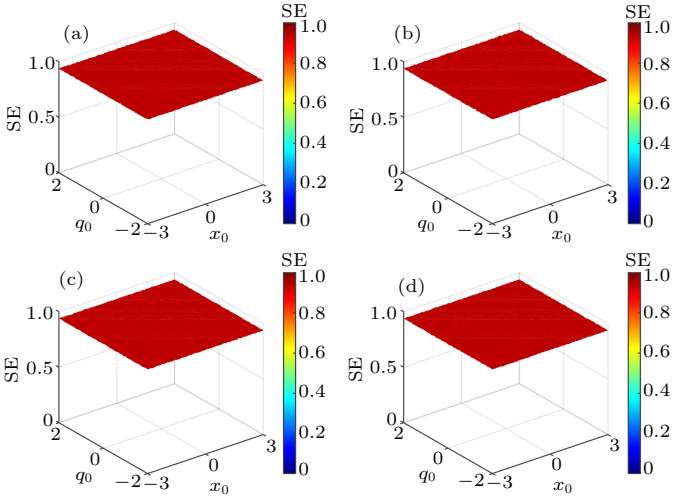


Fig. 11. The SE complexity of MBSC maps with $a = 3$, $b = 1$, $m = 2$, $k = 5$: (a) Q-MBSC map, (b) A-MBSC map, (c) S-MBSC map, (d) E-MBSC map.

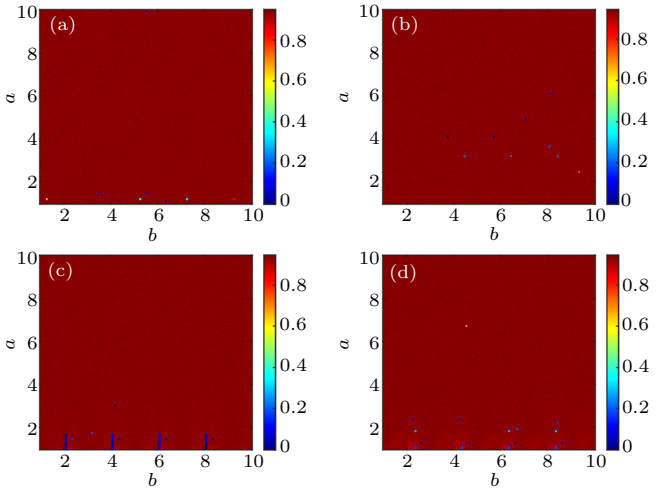


Fig. 12. SE complexity of MBSC maps with $k = 5$, $m = 2$, $x_0 = 0.1$, $q_0 = 0.1$: (a) Q-MBSC map, (b) A-MBSC map, (c) S-MBSC map, (d) E-MBSC map.

Furthermore, in Table 2, the maximum Lyapunov exponent and SE complexity of the DM map[16] and the MBC map,[37] as well as the MBSC map proposed in this paper, are listed under identical parameters. The parameter k of the DM map is equivalent to the parameter a of the MBC and MBSC maps. Comparison shows that under identical parameters, the Lyapunov exponent and SE complexity of the MBSC map are higher than those of the DM and MBC maps. The results indicate that the MBSC map has better chaotic performance.

Table 2. The structure of the MBSC method.

DM-based maps	Parameters setting	MLE	SE
Q-DM map[16]	$k = 1.78$	0.2741	0.8688
A-DM map[16]	$k = 2.3$	0.2561	0.7450
S-DM map[16]	$k = 1.84$	0.2582	0.8736
E-DM map[16]	$k = 2.66$	0.2513	0.8637
Q-MBC map[37]	$b = 1, m = 4, a = 1.78$	1.7185	0.9255
A-MBC map[37]	$b = 1, m = 4, a = 2.3$	1.1508	0.9324
S-MBC map[37]	$b = 1, m = 4, a = 1.84$	0.9616	0.9248
E-MBC map[37]	$b = 1, m = 4, a = 2.66$	1.1849	0.9261
Q-MBSC map	$b = 1, m = 4, a = 1.78, k = 5$	2.6896	0.9605
A-MBSC map	$b = 1, m = 4, a = 2.3, k = 5$	1.7341	0.9606
S-MBSC map	$b = 1, m = 4, a = 1.84, k = 5$	1.5138	0.9581
E-MBSC map	$b = 1, m = 4, a = 2.66, k = 5$	1.7738	0.9600

3.4. Chaotic region scale (CRS)

The CRS is a quantitative index designed to evaluate the chaotic range of chaotic systems.[41] It enables a quantitative analysis to determine the extent of the chaotic range, rather than merely making a qualitative judgment on whether the chaotic range is wider or narrower. The mathematical expression of CRS is as follows:

$$\begin{aligned} \mathrm{CRS} &= \frac{\sum_{i=1}^{l} (a_{ij}^{*} - a_{i0}^{*})/\Delta p}{(a_j - a_0)/\Delta p} \times 100\% \\ &= \frac{\sum_{i=1}^{l} (a_{ij}^{*} - a_{i0}^{*})}{(a_j - a_0)} \times 100\%. \end{aligned} \tag{4}$$

Here, a_0 and a_j represent the starting and cutoff parameters of the total parameter range, respectively. a_{i0}^{*} and a_{ij}^{*} are the starting and cutoff parameters of different chaotic parameter regions. l denotes the number of chaotic regions within the total parameter range, and Δp is the step accuracy. When conducting comparisons, reference should be made to the chaotic parameter region of the original system. Additionally, the compared systems must adopt the same step accuracy and parameter range.

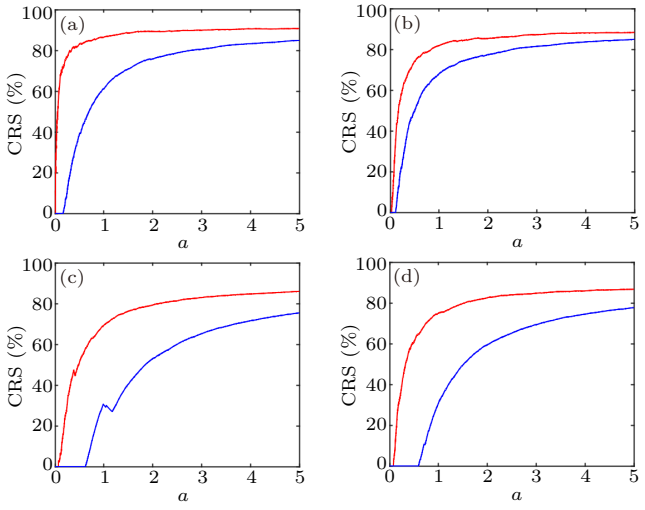


Fig. 13. The CRSs related to a: (a) Q-MBSC map and Q-MBC map, (b) A-MBSC map and A-MBC map, (c) S-MBSC map and S-MBC map, (d) E-MBSC map and DMP–MBC map (red: MBSC map, blue: MBC map).

We perform a comparative analysis of the CRS between MBSC maps and the maps from previous studies, with parameter a as the variable. The parameters are set as follows: $a_0 = 0$, $a_j = 5$, and step size $\Delta p = 0.01$. The comparison of CRS indices between the two types of models is presented in Fig. 13. As observed from the figure, the CRS index of the improved model is significantly higher than that of the MBC across the entire chaotic region, indicating that the MBSC effectively enhances the chaos range of the maps within the parameter domain.

4. PRNG design and test

4.1. PRNG design

PRNGs play a fundamental role in modern cryptographic systems by providing statistically random sequences from deterministic algorithms. The PRNG based on the MBSC map adopts a three-stage processing architecture to convert chaotic sequences into cryptographically secure random numbers. The specific implementation steps are as follows.

Step 1: The system implements the MBSC map with identical parameters. After performing 1000 warm-up iterations to eliminate transient effects, it generates two distinct chaotic sequences: x_n and q_n. The co-generated sequences provide complementary nonlinear characteristics for enhanced randomness in subsequent processing stages.

Step 2: The chaotic sequences undergo standardized numerical processing to ensure cryptographic-quality randomness. First, each 32-bit floating-point value x_n, q_n is converted to 32-bit IEEE 754 binary. The system then performs uniform bit extraction across all sequences using

$$\begin{cases} M_x = (\mathrm{bits}(x_n) \,\&\, 0x000\mathrm{FF}000) \gg 12, \\ M_q = (\mathrm{bits}(q_n) \,\&\, 0x0000\mathrm{FF}0) \gg 4, \end{cases} \tag{5}$$

where $\gg$ and $\ll$ denote right and left bit shifts, respectively. This extracts 8-bit segments from bits 12–19 of x_n and 4–11 of q_n. The extracted values are combined via an XOR operation

$$M_a = M_x \oplus M_q. \tag{6}$$

Step 3: To maximize randomness, the extracted 8-bit values undergo a two-layer diffusion process. First, intra-value diffusion is applied through cyclic bit operations

$$M_{\mathrm{diff}} = M_a \oplus (M_a \gg 3) \oplus (M_a \ll 2). \tag{7}$$

This operation creates nonlinear dependencies between adjacent bits. The diffused values are then grouped into 32-bit blocks and processed with a lightweight permutation

$$R_{\mathrm{out}} = (M_{\mathrm{diff}}^{i} \oplus M_{\mathrm{diff}}^{i-1}) + 0x9\mathrm{E}3779\mathrm{B}9. \tag{8}$$

4.2. NIST test for the PRNG

The NIST SP 800-22 test suite,[42] a widely recognized standard in the United States, provides a comprehensive set of statistical tests designed to evaluate the randomness quality of PRNGs. It verifies their resistance against various statistical attacks and ensures cryptographic-grade unpredictability. The evaluation metrics include both p-values and pass rates, which collectively determine whether a sequence meets the stringent randomness requirements. For Q-MBSC and E-MBSC, we set $a = 3$, $b = 1$, $m = 4$, $k = 5$ and initial conditions $x_0 = 0.1$, $q_0 = 0.1$. Our experimental results demonstrate that both Q-MBSC- and E-MBSC-based PRNGs successfully pass NIST tests, confirming their strong randomness properties and practical applicability for security-sensitive applications. The complete test results are presented in Table 3 for detailed comparison.

Table 3. Test results of NIST SP800-22.

Test index	Q-MBSC map			E-MBSC map		
	P_{value}	Pass rate	Result	P_{value}	Pass rate	Result
Frequency	0.4573	0.99	Passed	0.5372	0.98	Passed
Block frequency	0.8561	0.98	Passed	0.2248	0.99	Passed
Runs	0.3367	1	Passed	0.8915	1	Passed
Longest run	0.6423	0.97	Passed	0.3567	0.97	Passed
Binary matrix rank	0.4565	0.99	Passed	0.1029	0.99	Passed
FFT	0.9410	0.96	Passed	0.6783	0.96	Passed
Non-overlapping template	0.3264	0.98	Passed	0.0145	0.98	Passed
Overlapping template	0.9146	0.97	Passed	0.4321	0.97	Passed
Linear complexity	0.4184	0.99	Passed	0.7654	0.99	Passed
Serial (1st)	0.1679	0.98	Passed	0.2983	0.98	Passed
Serial (2nd)	0.0479	1	Passed	0.9237	1	Passed
Approximate entropy	0.3465	1	Passed	0.5548	1	Passed
Cumulative sums forward	0.5677	0.97	Passed	0.1876	0.97	Passed
Cumulative sums reverse	0.9648	1	Passed	0.6412	0.96	Passed
Random excursions	0.5579	0.99	Passed	0.4098	1	Passed
Random excursions variant	0.8697	1	Passed	0.6475	1	Passed

4.3. Performance analysis of PRNG

To verify the practicality of the proposed PRNG in engineering applications, its computational complexity and throughput are evaluated. The PRNG operates in three sequential stages: warm-up iteration, bit extraction, and diffusion processing. Its time and space complexities are analyzed as follows.

4.3.1. Time complexity

Assume that the length of the generated random sequence is N. Warm-up iteration: A fixed number of 1000 iterations is executed to eliminate transient effects, which is independent of N. Thus, the time complexity is O(1). Bit extraction: For each of the N groups of state variables (x_n, q_n), operations including 32-bit IEEE 754 floating-point format conversion, bit masking extraction, and XOR combination are performed. Each operation takes constant time, leading to an overall time complexity of O(N). Diffusion processing: Two sub-steps are involved. intra-value diffusion performs 3 cyclic shifts and XOR operations on each 8-bit M_a, with constant time per operation. 32-bit block permutation operates independently of block length. The total time complexity for this stage is O(N).

Combining all stages, the total time complexity of the PRNG is O(N), indicating linear time efficiency, which is suitable for large-scale random sequence generation.

4.3.2. Space complexity

The PRNG only requires storing a constant number of fixed-size variables, including state variables: x_n and q_n (32-bit floating-point each), intermediate variables: M_x, M_q, M_a, M_{diff} (8-bit each), and a 32-bit block cache, control parameters: a, b, m, k (32-bit each). It is independent of the sequence length N. The total storage requirement is approximately 240 bits (< 30 bytes), resulting in a space complexity of O(1). This ultra-low memory footprint makes the PRNG highly suitable for resource-constrained hardware implementations.

4.3.3. Throughput tests

To verify the engineering feasibility of the proposed PRNG, throughput tests were conducted under software simulation, where the PRNG was implemented in Python 3.9 and run on an Intel Core i5-12400 CPU (3.7 GHz). The throughput was evaluated by measuring the time required to generate a 1 GB random sequence. The result shows that the PRNG completed the generation in 27.8 seconds, corresponding to a throughput of 294 Mbps. This performance level demonstrates strong adaptability to practical application scenarios. It can provide sufficient redundancy for low-rate tasks, such as sensor data encryption (which typically requires 1–10 Mbps), and fully meets the bandwidth demands of medium-rate applications including image encryption (10–100 Mbps) and secure communication (50–500 Mbps). It ensures real-time sequence

generation without latency accumulation, confirming that the proposed PRNG balances efficiency and reliability in software implementation for a wide range of chaotic cryptography and secure communication scenarios.

5. Conclusions

In this paper, we propose a novel modular-bias-sin chaotification method to address the limitations of existing DM-based chaotic maps, such as constrained chaotic domains, small Lyapunov exponents, and insufficient complexity. By applying it to four fundamental DMs, we successfully construct the enhanced chaotic maps. The comprehensive dynamical analyses demonstrate that the MBSC-enhanced maps exhibit significant improvements, including wider chaotic parameter ranges, stronger chaotic intensity, higher complexity, and robustness to perturbations. Additionally, a PRNG based on the Q-MBSC and E-MBSC maps is implemented, which employs a three-stage processing architecture and passes all NIST SP 800-22 tests. Thus, the MBSC method effectively enhances the chaotic performance of DM-based maps while maintaining structural simplicity and implementation feasibility, showing promise for applications like image encryption and secure communication, with future work focusing on optimizing parameters, exploring hardware implementations, and extending the method to other chaotic systems.

Acknowledgement

This work was supported by the National Natural Science Foundation of China (Grant Nos. 62071496 and 62061008).

References

[1] Chua L O 1971 *IEEE Transactions on Circuit Theory* **18** 507
[2] Strukov D B, Snider G S, Stewart D R and Williams R S 2008 *Nature* **453** 80
[3] Shi L, Zheng G, Tian B, Dkhil B and Duan C 2020 *Nanoscale Advances* **2** 1811
[4] Ju D, Lee S, Lee J and Kim S 2024 *J. Alloys Compd.* **998** 174926
[5] Zhang Y P, Wang F, Shan X, Lin X, Zhao X Y, Zhou Q Z, Shan K, Ma Z X, Chen G, Wang X, Huang D C and Zhang K L 2023 *Materials Science and Engineering: B* **290** 116360
[6] Patil H, Kim H, Kadam K D, Rehman S, Patil S A, Aziz J, Dongale T D, Sheikh Z A, Rahmani M K, Khan M F and Kim D K 2023 *ACS Applied Materials & Interfaces* **15** 13238
[7] Wang H H, Chen H Q, Sun K H, Zhu W T and Yao Z 2025 *Nonlinear Dyn.* **113** 10365
[8] Yuan Z Y, Wu Y L, Ou C Y, Zhong P C, Zhao X and Ma M L 2025 *Chin. J. Phys.* **94** 108
[9] Liao Z C, Ouyang J P and Ma M L 2025 *Nonlinear Dyn.* **113** 12151
[10] Ding Y, Liu W H, Wang H H and Sun K H 2023 *Euro. Phys. J. Plus* **138** 638
[11] Liu X K, Sun K H and Wang H H 2024 *Euro. Phys. J. Plus* **139** 27
[12] Yang F F, Ren L J, Ma J and Zhu Z G 2024 *Journal of Zhejiang University-Science A* **25** 382
[13] Li Y X, Li C B, Lei T F, Yang Y and Chen G R 2023 *IEEE Transactions on Industrial Electronics* **71** 9569
[14] Peng Y X, Sun K H and He S B 2020 *Chaos, Solitons & Fractals* **137** 109873
[15] Wang H H, Li G, Sun K H and He S B 2024 *Eur. Phys. J. Plus* **139** 154
[16] Bao H, Hua Z Y, Li H Z, Chen M and Bao B C 2021 *IEEE Transactions on Circuits and Systems I: Regular Papers* **68** 4534
[17] Bao H, Hua Z Y, Wang N, Zhu L, Chen M and Bao B C 2021 *IEEE Transactions on Industrial Informatics* **17** 1132
[18] Dong Q Q, Bai Y L and Zhu K L 2024 *Physica Scripta* **99** 035253
[19] Xu Q, Huang L P, Wang N, Bao H, Wu H G and Chen M 2023 *Nonlinear Dyn.* **111** 20447
[20] Liu W H, Sun K H, Wang H H, Li B L and Chen Y J 2024 *IEEE Transactions on Circuits and Systems I: Regular Papers* **72** 254
[21] Ramakrishnan B, Njimah O M, Kengne J and Rajagopal K 2022 *Eur. Phys. J. Plus* **137** 787
[22] Yan X, Li Z J and Li C L 2024 *Chin. Phys. B* **33** 028705
[23] Lu J Y, Xie X H, Lu Y P, Wu Y L, Li C L and Ma M L 2024 *Chin. Phys. B* **33** 048701
[24] Liu T M, Mou J, Li X, Han X T, Yan H Z and Cao Y H 2021 *Physica Scripta* **96** 125242
[25] Bao B C, Rong K, Li H Z, Li K X, Hua Z Y and Zhang X 2021 *IEEE Transactions on Circuits and Systems II: Express Briefs* **68** 2992
[26] Bao H, Hua Z Y, Li H Z, Chen M and Bao B C 2021 *IEEE Transactions on Industrial Informatics* **18** 5297
[27] Ma M Y, Yang Y, Qiu Z C, Peng Y X, Sun Y C, Li Z J and Wang M J 2022 *Nonlinear Dyn.* **107** 2935
[28] Liang Z W, He S B, Wang H H and Sun K H 2022 *Eur. Phys. J. Plus* **137** 309
[29] Fu L X, Wu X M, He S B, Wang H H and Sun K H 2023 *IEEE Transactions on Industrial Electronics* **71** 9668
[30] Wang H H, Li G, Sun K H and He S B 2024 *Euro. Phys. J. Plus* **139** 154
[31] Wu W P, Wang M J and Yang Q G 2025 *Chin. Phys. B* **34** 050503
[32] Bao H, Gu Y, Xu Q, Zhang X and Bao B C 2022 *Chaos, Solitons & Fractals* **160** 112273
[33] Gu Y, Bao H, Xu Q, Zhang X and Bao B C 2023 *IEEE Transactions on Circuits and Systems II: Express Briefs* **70** 3109
[34] Yuan F, Xing G B and Deng Y 2023 *Chaos, Solitons & Fractals* **166** 112888
[35] Deng Y and Li Y X 2021 *IEEE Transactions on Circuits and Systems II: Express Briefs* **69** 1817
[36] Yu X, Bakar A A, Li K S, Wang Q and Sang H W 2024 *Physica Scripta* **99** 075218
[37] Wang H H, Zhu H H, Li B L, Sun K H and Liu W H 2024 *Eur. Phys. J. Plus* **139** 826
[38] Liu J, Sun K H and Wang H H 2024 *Chaos* **34** 083102
[39] Laskaridis L, Volos C, Giakoumis A E, Meletlidou E and Stouboulos I 2025 *Electronics* **14** 311
[40] Wang M J, An M Y, Zhang X N and Iu H H C 2023 *IEEE Transactions on Circuits and Systems II: Express Briefs* **70** 4251
[41] Zhu H H, Liu W H, Sun K H and Wang H H 2025 *Nonlinear Dyn.* **113** 26773
[42] Pareschi F, Rovatti R and Setti G 2012 *IEEE Transactions on Information Forensics and Security* **7** 491